Novel Core–Shell Polyamine Phosphate Nanoparticles Self-Assembled from PEGylated Poly(allylamine hydrochloride) with Low Toxicity and Increased In Vivo Circulation Time

Patrizia Andreozzi, Cristina Simó, Paolo Moretti, Joaquin Martinez Porcel, Tanja Ursula Lüdtke, Maria de los Angeles Ramirez, Lorenza Tamberi, Marco Marradi, Heinz Amenitsch, Jordi Llop, Maria Grazia Ortore, and Sergio Enrique Moya*

An approach for reducing toxicity and enhancing therapeutic potential of supramolecular polyamine phosphate nanoparticles (PANs) through PEGylation of polyamines before their assembly into nanoparticles is presented here. It is shown that the number of polyethylene glycol (PEG) chains for polyamine largely influence physico-chemical properties of PANs and their biological endpoints. Poly(allylamine hydrochloride) (PAH) are functionalized through carbodiimide chemistry with three ratios of PEG molecules per PAH chain: 0.1, 1, and 10. PEGylated PAH is then assembled into PANs by exposing the polymer to phosphate buffer solution. PANs decrease size and surface charge with increasing PEG ratios as evidenced by dynamic light scattering and zeta potential measurements, with the ten PEG/PAH ratio PANs having practically zero charge. Small angle X-ray scattering (SAXS) proves that PEG chains form a shell around a polyamine core, which is responsible for the screening of positive charges. MTT experiments show that the screening of amine groups decreases nanoparticle toxicity, with the lowest toxicity for the 10 PEG/PAH ratio. Fluorescence correlation spectroscopy (FCS) proves less interaction with proteins for PEGylated PANs. Positron emission tomography (PET) imaging of ^{18}F labelled PANs shows longer circulation time in healthy mice for PEGylated PANs than non-PEGylated ones.

1. Introduction

Polyamine phosphate nanoparticles (PANs) are supramolecular assemblies of poly(allylamine hydrochloride) (PAH) and phosphate ions,[1–5] which display a fascinating response to variations in pH.[6] PANs are stable at neutral and moderately basic pH values, from 7 to 9. Outside of this narrow pH range, PANs disassociate into their molecular components. This pH-responsiveness makes PANs a very appealing vehicle for intracellular drug delivery, as they are stable in physiological media and pH values, but disassemble inside endosomes, that is, at pH below 6, liberating encapsulated cargo.[7] Besides, the amine groups in the polyamines can protonate inside endosomes, inducing an osmotic swelling that facilitates PANs translocation into cytosol. In a recent paper, we have explored the use of PANs prepared with PAH for the delivery

Dr. P. Andreozzi, C. Simó, Dr. J. Martinez Porcel, T. U. Lüdtke, M. A. Ramirez, L. Tamberi, Dr. S. E. Moya
Soft Matter Nanotechnology Group
CIC biomaGUNE
Basque Research and Technology Alliance (BRTA)
Paseo Miramón 182, San Sebastián, Guipúzcoa 20014, Spain
E-mail: smoya@cicbiomagune.es

Dr. P. Andreozzi
Consorzio Sistemi a Grande Interfase
Department of Chemistry 'Ugo Schiff'
University of Florence
Via della Lastruccia 3, Sesto Fiorentino, Florence 50019, Italy

C. Simó, Dr. J. Llop
Radiochemistry and Nuclear Imaging Group
CIC biomaGUNE
Basque Research and Tech-nology Alliance (BRTA)
Paseo Miramón 182, San Sebastián, Guipúzcoa 20014, Spain

Dr. P. Moretti, Dr. M. G. Ortore
Dipartimento di Scienze della Vita e dell'Ambiente
Università Politecnica delle Marche
Via brecce bianche, Ancona I-60131, Italy

M. A. Ramirez
Instituto de Nanosistemas
UNSAM
CONICET
Avenida 25 de Mayo 1021, San Martín, Buenos Aires 1650, Argentina

Dr. M. Marradi
Department of Chemistry 'Ugo Schiff'
University of Florence
Via della Lastruccia 3/13, Sesto Fiorentino, Florence 50019, Italy

Dr. H. Amenitsch
Institute of Inorganic Chemistry
Graz University of Technology
Stremayergasse 9/V, Graz 8010, Austria

Dr. J. Llop
Centro de Investigación Biomédica en Red – Enfermedades Respiratorias (CIBERES)
Av. Monforte de Lemos, 3–5, Madrid 28029, Spain

of siRNAs and we have shown that PANs are capable of successfully silencing green fluorescent protein expression at nontoxic concentrations.[6] An increase in PANs concentration, however, which could be expected to lead to a more effective silencing, resulted in moderate toxicity, thereby limiting therapeutic use.

PAH toxicity is associated with the presence of primary amines.[8–10] Reducing the toxicity of PANs should increase their potential for drug delivery and facilitate their clinical translation. A common procedure to increase biocompatibility of nanoparticles is the use of coatings based on antifouling molecules such as polyethylene glycol (PEG) that is highly hydrated but uncharged and displays limited interaction with biomolecules and cells.[11–13] PEG coatings have been extensively used to prolong circulation time of nanoparticles and for generating antifouling surfaces. The modification of inorganic nanoparticles with PEG molecules is frequently performed post synthesis, which often results in limited control of the density of the PEG chains around the nanoparticles.[14] On the other hand, for polymeric nanoparticles or micelles PEG is in most cases linked to another polymer, as a copolymer, or to surfactants before nanoparticle or micelle formation, respectively.[15,16] PEG density[17] is determinant on the interaction with proteins, and for screening against positive charges.[18] A dense PEG coating around nanoparticles prevents the opsonization process from taking place during circulation, limiting recognition by the mononuclear phagocyte system (MPS), and prolonging circulation time. This, ultimately, contributes to a sustained and prolonged delivery of therapeutic drugs and increases the targeting efficacy of nanoparticles to reach specific organs.[19]

Because PANs are formed by polyamines, they display free accessible amines on their surface, which can be easily modified with COOH-functionalized PEG by carbodiimide chemistry. However, PAH can also be functionalized with PEG chains prior to nanoparticle formation. In this study we chose to follow the second approach, with the aim of gaining control over chains density of PEG on the nanoparticles. Hence, we have modified PAH with PEG chains, and unreacted amine groups were used to form nanoparticles through complexation with phosphates. While the association of PAH chains trough phosphate was not prevented by PEGylation, we have observed by dynamic light scattering (DLS), zeta potential measurements, and small angle X-ray scattering (SAXS) that the number of PEG molecules per PAH chain play a fundamental role in the organization of the polyamines into PANs, leading to a core–shell structure with PEG forming a shell around a polyamine core. PEG chains impose steric constraints that affect the size of the PANs and the capacity of association among polymer chains. Depending on the number of PEG chains per polyamine different assemblies are formed with nonidentical properties. As the number of PEG chains increase per polyamine the PEG coating becomes denser and the nanoparticle decrease in size. Interestingly, we observed that PANs retain their ability to disassemble at endosomal pH values, despite changes in their physico-chemical characteristics. PEGylation of PAH affects PANs–protein interactions as observed by fluorescence correlation spectroscopy (FCS).[20] Moreover, PEGylated PANs show a decreased toxicity as evaluated with the MTT assay, and longer circulation times as

determined by positron emission tomography (PET), which enhance their potential for drug delivery applications.

To resume, we show here novel PEGylated assemblies fabricated through covalently modifying polyamines and inducing their association with phosphate ions, and we have been able to correlate the organization of the PEGylated polyamine chains with the physico-chemical properties and toxicological endpoints of the assemblies.

2. Results and Discussion

PAH molecules were conjugated with PEG-hydroxysuccinimide through amide formation. Synthetic conditions for PEGylation are detailed in the experimental section. After PEGylation of PAH, PANs were formed by addition of PBS to the polymer solutions. PEG chains were attached to PAH molecules with three different ratios of PEG per PAH chain (PEG_x:PAH): 01, 1, and 10, which are named $PEG_{0.1}$:PAH, PEG_1:PAH, and PEG_{10}:PAH, respectively. The PEGylation reaction is shown in **Scheme 1**, as well as a sketch of the different PANs obtained exposing PEG_x:PAH to phosphate buffer, according to the number of PEG chains per PAH.

The PEG_x:PAH ratio was confirmed by NMR (see Figure S1, Supporting Information). The formation of PANs with PEGylated PAH was characterized by DLS, transmission electron microscopy (TEM), zeta potential measurements, and SAXS. DLS shows that the size of the PANs decreases as the number of PEG chains per PAH chain increases, for the same PBS concentration and ionic strength (**Figure 1**). In the case of $PEG_{0.1}$:PAH, the hydrodynamic diameter of the PEGylated PANs is the same as for PANs formed by PAH (non-PEGylated), approximately 125 nm, and decreases to ≈60 nm for PEG_1:PAH and to about 25 nm for PEG_{10}:PAH. TEM images of PEGylated PANs confirm a well-defined spherical shape and an average diameter of around 25 nm (Figure 1; Figure S2, Supporting Information). Both TEM and DLS measurements evidence that PEGylation does not prevent PAN formation, although it has a clear influence on particle size. Additionally, PEGylation does not prevent the characteristic response of PANs with pH.
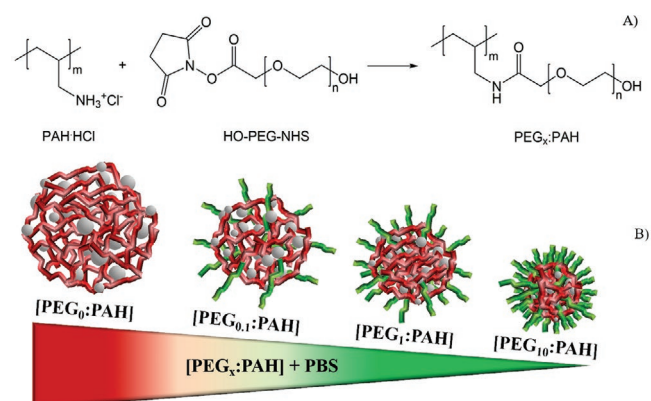
Scheme 1. Synthetic procedure followed for the preparation of the PEGylated PAH NPs. On top PEGylation of PAH. On the bottom, scheme of the PANs obtained for the different PEG_x:PAH polymers in presence of PBS.
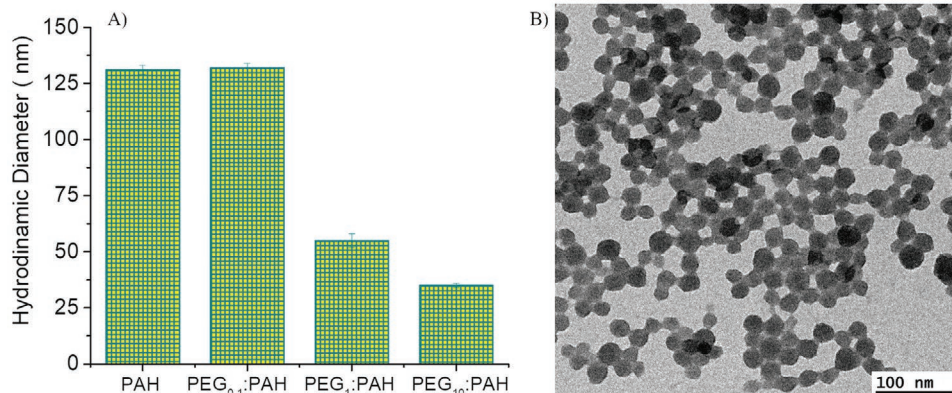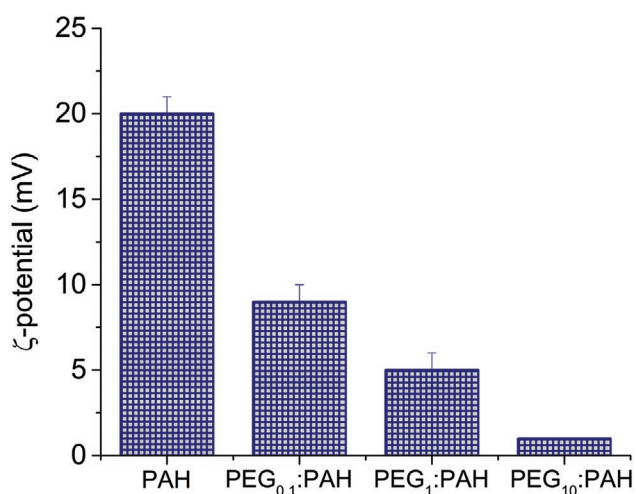
Figure 1. A) Hydrodynamic diameter obtained by DLS as a function of different molar ratio at 1 mg mL⁻¹ of PEG$_x$:PAH in 5 mM phosphate buffer (PB). B) TEM image of PEGylated PANs obtained with PEG$_{10}$:PAH ratio in PB 5 mM.

DLS shows that PEGylated PANs disassemble at pHs around 5, where counts are practically 0, meaning that there are no scattering objects in solution (Figure S3, Supporting Information).

The attachment of uncharged PEG chains has also an impact on particle charge. ζ-potential measurements show a decrease in the ζ-potential of PANs as the number of PEG chains per PAH increases, from +20 mV for the unmodified PANs to less than +5 mV for both PEG$_1$:PAH and PEG$_{10}$:PAH (**Figure 2**). ζ-potential values below +5 mV can actually be considered 0, suggesting that the charges from PAH are completely, or almost completely, screened by the PEG chains. The formation of a PEG shell around the PANs that screens positive charges from PAH would explain both the decrease in ζ-potential with PEGylation and the decrease in the size of the PANs with increasing number of PEG chains per PAH molecule. This is likely due to the arrangement of the PEG chains limiting the interaction of non-PEGylated segments of PAH and imposing steric constraints for nanoparticle formation and growth.

SAXS measurements were conducted to prove the hypothesis of a core–shell structure for the PEGylated PANs. SAXS provides information regarding average dimensions of particles in solution and their structural features. While DLS provides the number density of spherical nanoparticles and their size distribution around an average value, through SAXS measurements it is possible to distinguish polymers with different electron densities; hence, they can be used to prove a different spatial organization of PAH and PEG inside the nanoparticles.

SAXS measurements were performed with PANs prepared with the three PEG$_x$:PAH ratios and with different phosphate buffer concentrations and ionic strengths. The experimental set up in the synchrotron SAXS allows us to accurately determine the size of PANs and their PEGylated shell, considering fixed values of the electron density of both polymers in all the experimental conditions as taken from literature.[21,22] Experimental data can be then fitted assuming a core–shell structure with a core with the electronic density of PAH and the shell with that of PEG (**Figure 3**).

From SAXS data analysis, a clear trend in nanoparticle size as a function of PEG$_x$:PAH can be observed. In fact, as the PEG$_x$:PAH ratio increases, PAN's dimensions decrease, in agreement with DLS results, **Figure 4**A. For the smallest PEG$_x$:PAH ratio, 0.1, an increase in size of about a 30% was observed when PBS concentration increased from 2 to 10 mM. The variations in size for PANs with PBS were less significant for PEG$_1$:PAH, as observed by DLS (data not shown), and negligible for PEG$_{10}$:PAH. For PANs self-assembled by PEG$_{10}$:PAH, size remains almost constant with increasing PBS concentration. The different size dependences on PBS concentration for the three PEG:PAH ratio can be explained considering that as the number of PEG chains per PAH molecule increases, the number of chains of PAH that can be associated in the PANs must decrease to cope with the constraint of arranging PEG chains on the surface of the PANs. The arrangement of PEG chains hinders the increase of the nanoparticles with PBS. In the case of non-PEGylated PANs an increase in PBS concentration allows for more PAH chains to associate, triggering particle grow. For the PEG$_{0.1}$:PAH ratio, since there is one PEG chain every ten PAH chains, we observe that the concentration of PBS still influences particle growth. One PEG chain every ten chains of PAH is easy to accommodate on the surface of the PANs. For the PEG$_{0.1}$:PAH one must think in discrete PEG chains, not forming a complete coating and the addition of one

Figure 2. ζ-potential (mV) of PANs as a function of different molar ratio of PEG, PEG$_x$:PAH.
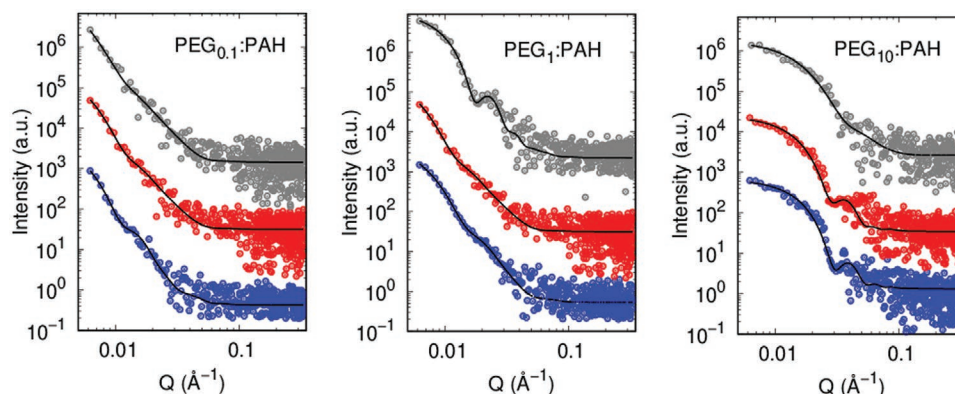
Figure 3. On the left: panel of SAXS experimental curves with their theoretical fitting obtained by GENFIT. SAXS curves (scaled for clarity) in blue, red, and grey correspond to PANs prepared with of 2, 5, and 10 mM PBS, respectively.

PEG chain to the nanoparticle would allow for the assembly of nine additional non-PEGylated PAH chains per particle. As the number of PEG chains increases per PAH chain, more PEG molecules have to be accommodated on the surface of the PANs. For 1 PEG chain per PAH each chain in the nanoparticle has to be arranged in such a way that the PEG remains in the outer region of the PAN, which limits the number of chains to be associated and imposes topological constraint for the arrangement of the polymers through phosphate ions. For 10 PEG per PAH chain the number of PEG chains to accommodate is even larger. One additional chain of polymer in the PAN would imply 10 PEG chains more to be located on the surface of the nanoparticles. Besides, there is the additional difficulty for the association of non-PEGylated segments of the polymer while arranging the PEG chains on the surface. Besides, there is the additional difficulty for the association of non-PEGylated segments of the polymer while arranging the PEG chains on the surface. Amine groups from different polyamine chains or from the same polyamine chain must be in close vicinity to associate through phosphate groups. The presence of 10 PEG
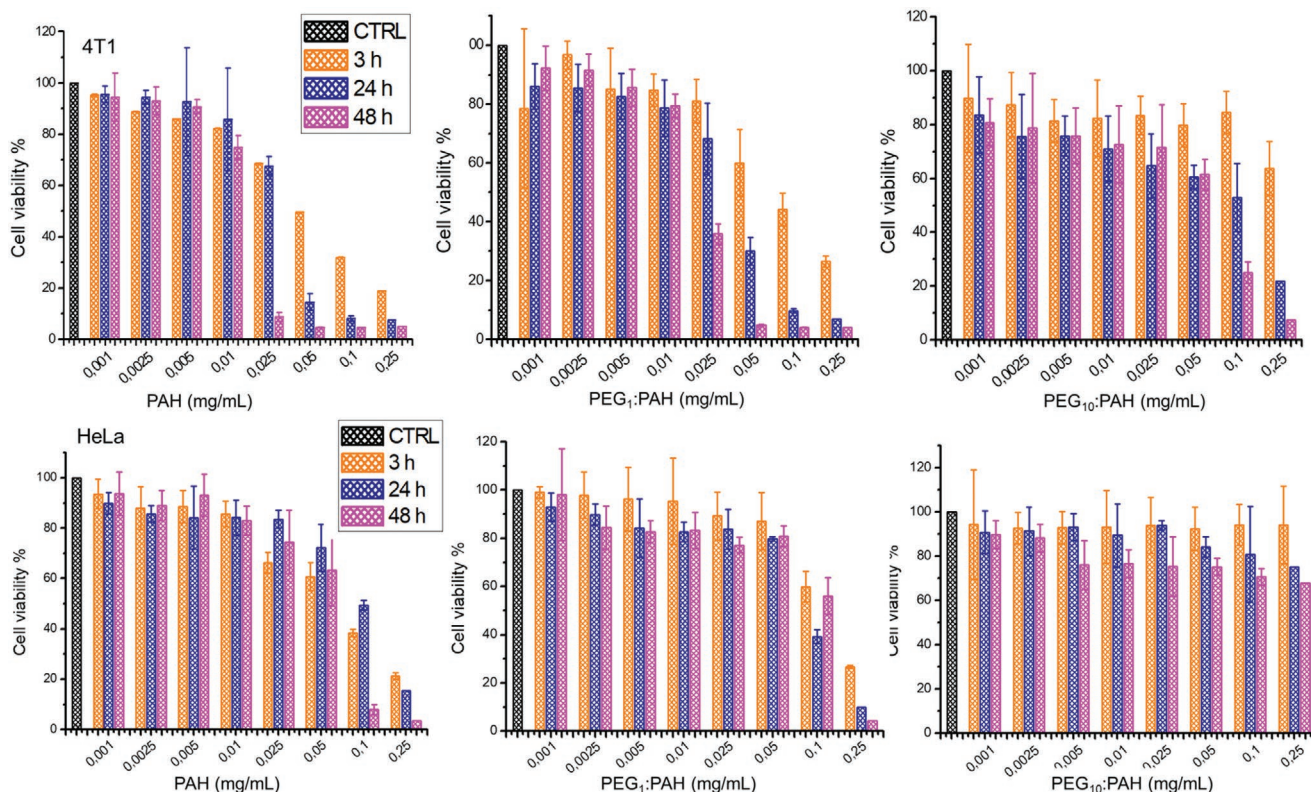
chains in a PAH chain difficult that segments with free amines come together as the PEG act as a steric barrier.

A similar rationale can be applied for the ionic strength. For non-PEGylated PANs, increasing the ionic strength results in more coiled conformations for the polyamines and in less electrostatic repulsion among them, favoring the growth of larger particles. Ionic strength should have less impact on conformation of PEGylated PAH chains as the PEG side chains are not charged. Therefore, the steric constraints imposed by the PEG chains should not be affected by the ionic strength. The larger the number of PEG chain per PAH molecule, the weaker is the influence of the ionic strength on particle size (data not shown).

Thickness of the PEG shell obtained from SAXS data has been plotted as a function of the PEG$_x$:PAH ratio and PBS concentration (Figure 4B). Increasing the number of PEG chains per PAH molecule results in a decrease in thickness of the PEG shell, with the thinnest PEG shells observed for PEG$_{10}$:PAH. For this number of PEG chains, ζ-potential values suggested the presence of a denser PEG shell. Taking together DLS and SAXS results, it is possible to understand the decrease in
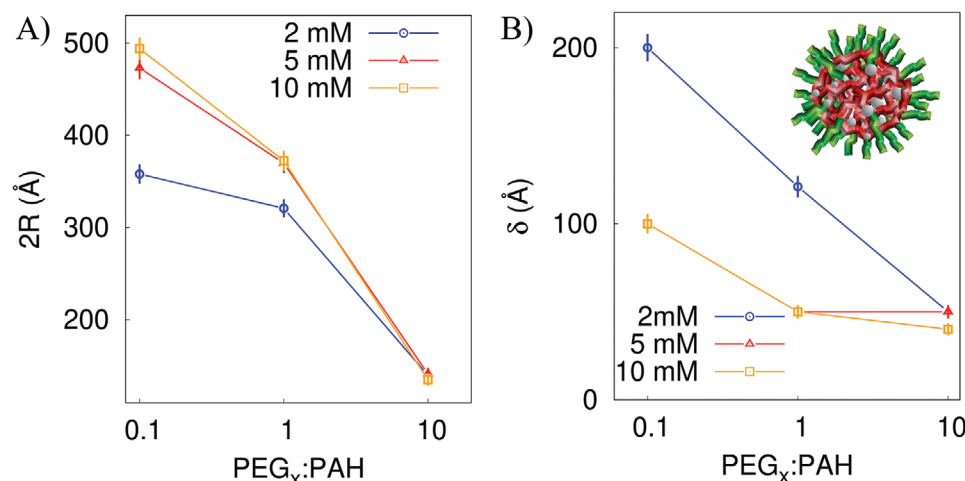
Figure 4. A) PEG$_x$:PAH NPs average radius as a function of PBS concentration and of PEG:PAH ratio resulting from SAXS data fitting. The legend details the phosphate buffer content. Lines are guide to the eyes. B) Thickness of PEG shell as a function of PBS content, as reported in the legend, and of PEG$_x$:PAH ratio.

ADVANCED
SCIENCE NEWS
www.advancedsciencenews.com

NANO · MICRO
small
www.small-journal.com

Figure 5. MTT assay for measuring cell proliferation after exposure to PANs and PEGylated PANS with the three PEG$_x$:PAH for 2 cell lines. Polymer concentration varied from 0.001 to 0.25 mg mL^{-1} at different time points, 3, 24, and 48 h as indicate in the legend. Black bar refers to untreated cells.

thickness with increasing number of PEG chains considering that the steric constraints of PEG$_{10}$:PAH leads to a smaller association of PAH chains, and in this situation the total number of PEG chains on the surface of the nanoparticle may be less than at 0.1 and 1 PEG$_x$:PAH ratios, resulting in a smaller thickness of the PEG shell. However, since the size of the PAH core is also small for the PEG$_{10}$:PAH ratio, the screening of the charged core is more effective. PEGylation of PAH did not prevent the polyamines from assembling while at the same time succeed in screening positive charges from amines. The screening of positive charges can have an impact on toxicological endpoints of the PANs and in their biological fate.

In order to assess toxicity after PEGylation, the MTT assay was conducted for three immortalized cell lines, Hela,4T1, and A549 at three time points: 3, 24, and 48 h. Cell proliferation studies are shown in **Figure 5** for HeLa and 4T1 cells. HeLa cells are less affected than 4T1 cells by PANs in their proliferation. In case of HELA cells, control nanoparticles (unmodified PANs) and PANs with a PEG$_{0.1}$:PAH ratio have no significant impact on proliferation up to a concentration of 0.05 mg mL^{-1} (concentration refers to the total polymer content), irrespectively of the time point considered (Figure 5; Figure S4, Supporting Information). Above this concentration, proliferation decreases below 50% for the unmodified PANs and PEG$_{0.1}$:PAH while it remains high for PEG$_1$:PAH and PEG$_{10}$:PAH. In the case of PEG$_1$:PAH, an increase in polymer concentration results in a progressive decrease in proliferation. At 0.1 mg mL^{-1} PEG$_1$:PAH PANs reduce cell proliferation to a 50% and

can be therefore already considered toxic. At 0.25 mg mL^{-1} PEG$_1$:PAH PANs, cell proliferation is low, comparable with the proliferation in the presence of non-PEGylated PANs and PEG$_{0.1}$:PAH PANs. This behavior is observed for the three time points considered. For PEG$_{10}$:PAH PANs, cell proliferation is practically unaffected for all concentrations studied at the three time points.

For 4T1 cells we observe that while at low PAN concentrations, cell proliferation is similar to that of HELA cells, when PAN concentration increases cells become more sensitive to the nanoparticles. At 3 h, all PANs can be considered nontoxic up to concentrations of 0.025 mg mL^{-1}. At 0.1 mg mL^{-1} proliferation decreases to 50% for non-PEGylated PANs, PEG$_{0.1}$:PAH, and also for PEG$_1$:PAH. Overall, PEG$_1$:PAH PANs result in a decreased cell proliferation in this cell line compared with the HeLa cell line. At 24 h we observe that the PEG$_1$:PAH PANs are already toxic at 0.05 mg mL^{-1}, with a cell proliferation of less than 40%. For PEG$_{10}$:PAH PANs, cell proliferation is less affected. At 3 h, only at the highest concentration, 0.25 mg mL^{-1}, cell proliferation values approach 50%, hinting to a toxic effect. After 24 h, 50% proliferation can be observed for 0.1 mg mL^{-1} PANs, and less than a 20% proliferation for 0.25 mg mL^{-1}. A549 cells show the same trend in proliferation as HeLa cells (Figure S5, Supporting Information).

It can be concluded that PEGylation of PAH has a positive effect on cell proliferation compared with non-PEGylated PANs. The lower toxicity after PEGylation of PANs can be explained by the screening of positive charges from the PEG shell around

ADVANCED
SCIENCE NEWS
www.advancedsciencenews.com

NANO · MICRO
small
www.small-journal.com
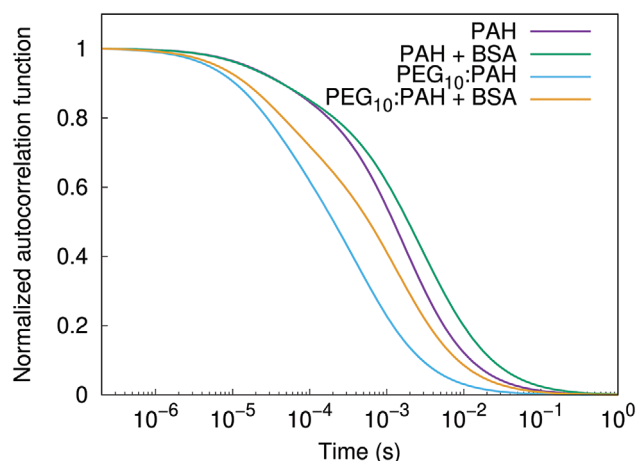
Figure 6. Autocorrelation functions obtained from fluorescence correlation spectroscopy from labelled non-PEGylated PANs (violet,) and PEG$_{10}$:PAH PANs (cyan), and in presence of 800 μM BSA in PBS (green for non-PEGylated PANs and yellow for PEG$_{10}$:PAH PANs).

the nanoparticles, as shown by ζ-potential measurements, which hinted a negligible surface charge for the PEG$_1$:PAH and PEG$_{10}$:PAH ratios. However, it must as well be considered that there is a reduction of the number of charges per mg of polymer when we use PEGylated PAH, which is more evident for the PEG$_{10}$:PAH ratio.

An important aspect of the PEG shell is its capacity to prevent, or decrease, the interaction with proteins, which can have large impact on PANs recognition by the immune system, and also in their translocation at tissue and cell levels.[23] To assess the interaction of PEGylated PANs with proteins, we performed a fluorescence correlation spectroscopy (FCS) study. This technique allows tracing the diffusion of fluorescent molecules, or objects, by recording fluctuations in fluorescence intensity within a confocal volume.[24,25] PAH chains were fluorescently labelled prior to PEGylation. Experiments were performed for non-PEGylated PANS and PEG$_{10}$:PAH PANs. The fluorescently labelled PANs were exposed in situ in the confocal microscope to 800 μM bovine serum albumin (BSA) proteins solution, to simulate physiological conditions. An increase in diffusion time for non-PEGylated and PEG$_{10}$:PAH PANs was observed in the presence of BSA, as shown by the autocorrelation functions in **Figure 6**. The increase in diffusion time is associated with the interaction of proteins with the PANs forming a protein corona. From the diffusion time, the size of the PANs before and after exposure to the proteins can be estimated, and although size changes for both PAN types, there is a much larger increase in particle diameter for non-PEGylated PANs compared to PEGylated ones, that is, an increase in 29.6 nm for the non-PEGylated PANs and 10.4 nm for the PEGylated (see Table S1, Supporting Information). PANs are exposed to BSA without removing excess of proteins from the media before FCS measurements. In this condition the formation of a soft protein corona around the PANs can be expected, meaning that not only the strongly bound (hard corona), but also proteins weakly bound will be affecting the diffusion of the PANs. This is the reason why a relatively large increase in size of the PANs with BSA is observed. Such an

increase in size may also mean a certain degree of aggregation; however, this cannot be concluded from the amplitude of the correlation functions. To conclude, PEGylated PANs show less association with proteins than non-PEGylated ones; still, proteins bind around the PEGylated PANs, which may indicate that there is enough free space between PEG chains to access to amine groups.

PET-CT studies were conducted in order to investigate the in vivo biodistribution of [18F]-labelled PANs prepared with PAH and PEG$_{10}$:PAH. Radiolabeling was performed as described in the experimental section through conjugation of a pre-labelled prosthetic group, [18F]F-PyTFP, to free amines in PAH and PEG$_{10}$:PAH. A radiochemical yield of 50% (with respect to [18F]F-PyTFP, decay-corrected, was achieved after 5 min incubation at room temperature of PAH or PEG$_{10}$:PAH with [18F]F-PyTFP. Radiochemical purity after purification was ≥99% for both cases, as determined by instant thin layer chromatography. Animals were injected with equal concentrations of either PANs or PEGylated PANs. From PET images, **Figure 7**A and the whole body reconstruction of PET-CT images shown in Figure 7B at 240 min a different distribution of the PEGylated and non-PEGylated PANs in the animal body can be clearly observed. The concentration of radioactivity as a function of time per organ was then evaluated and is shown in Figure 7C.

At short times after administration, non-PEGylated PANs show higher accumulation in the lungs and the liver than PEGylated PANs, while PEGylated PANs accumulate more in the heart during the first 25–30 min. At longer times, activity in the heart is higher for the non-PEGylated PANs, while to a large extent PEGylated PANs tend to accumulate in the bladder. The higher activity in the heart for the PEGylated PANs suggest a higher concentration of the PANs in blood. The progressive increase of radioactivity in the bladder is indicative of the PEGylated PANs being eliminated by urine. Biodistribution data shows that the PEGylated PANs have a longer circulation time compared to the non-PEGylated PANs and are more easily excreted through urine. These results are in agreement with the expected effect of PEGylation, which increases the circulation of nanoparticles by avoiding clearance by the mononuclear phagocyte system. The higher percentage of PEGylated PANs in the bladder and elimination through urine is likely related to the smaller size of these nanoparticles compared to the non-PEGylated ones.

3. Conclusions

PEGylation of PAH molecules does not prevent formation of PANs in presence of phosphate buffer but largely affects size and charge of the formed nanoparticles. Increasing the number of PEG chains per PAH molecule from 0.1 to 10 results in progressive decrease of the size and zeta potential of the nanoparticles, with zeta potential becoming practically 0 for 10 PEG chains per PAH. At this ratio of PEG to PAH the size of PANs decrease to 10 nm and size is practically not affected by PBS concentration. This decrease in size can be understood as a result of the topological constraints to accommodate the PEG chains while free amino groups from different polymer chains associate through interaction with phosphates.

ADVANCED
SCIENCE NEWS
www.advancedsciencenews.com

NANO · MICRO
small
www.small-journal.com
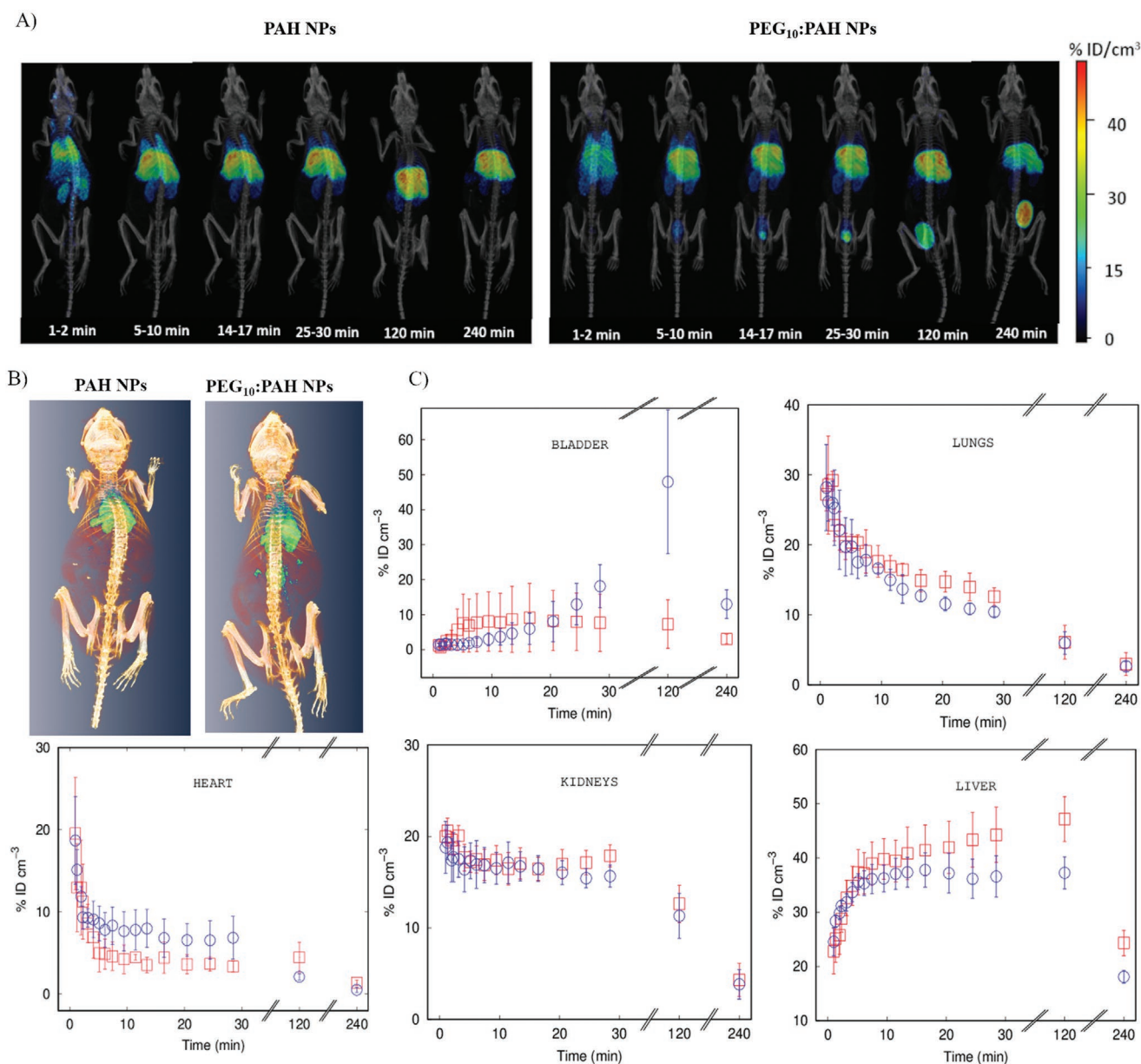
Figure 7. Biodistribution of ^{18}F-PAH/PEG:PAH NPs injected intravenously in female mice; A). Sequence of PET-CT images (maximum intensity projections) obtained at different time points; color regions show concentration of radioactivity. The scale on the right correlates activity intensity with percentage of injected dose per cm^3 (%ID cm^{-3}). B) Three dimensional reconstruction of the PET-CT images of the biodistribution of non-PEGylated PANs and PEG$_{10}$:PAH PANs at 240 min. C) Accumulation of non-PEGylated ^{18}F-PAH and ^{18}F-PEG:PAH NPs in different organs at different time points, as determined by PET imaging. Results are expressed as % of injected dose per gram. Error bars correspond to the mean ± standard deviation ($n = 3$ per NP type). Red dots refer to PEG$_{10}$:PAH NPs, violet dot to non-PEGylated NPs.

PANs with 10 PEG molecules per PAH chain display a core–shell structure with PEG chains forming the external shell as shown by SAXS measurements. The organization of PEG chains as a shell around a polyamine core is responsible of shielding positive charges from PAH as observed by zeta potential measurements and results in a decrease particle toxicity. PEGylation of PANs reduces interactions as well with proteins and prolong PANs circulation in vivo. Overall, we have shown here that by PEGylating PAH PANs characteristics are largely changed, with a shielding of positive charges in PANs as result of the presence of PEG as external shell, and enhancing PANs potential for biomedical applications by decreasing toxicity and extending nanoparticle circulation.

4. Experimental Section

Materials: Poly(allylamine hydrochloride) salt (PAH) (M_W:15×10^4 g mol^{-1}), phosphate buffer salt tablets (PBS), sodium phosphate dibasic (Na$_2$HPO$_4$), potassium phosphate monobasic (KH$_2$PO$_4$), hydrochloric

acid (HCl), sodium hydroxide (NaOH), and sodium chloride (NaCl), NHS-PEG-OH (5000 Da), all from Sigma-Aldrich, were used as received. Polyelectrolyte stock solutions and all subsequent diluted precursor solutions were prepared with MilliQ deionized water. Human lung adenocarcinoma (A549 CCL-185), breast cancer (4T1), HeLa cell lines were purchased from the American Type Culture Collection (ATCC, USA). RPMI and DMEM medium were purchased from Lonza (USA). 3,4,5-dimethylthiazol-2,5 biphenyl tetrazolium bromide (MTT), Penicillin-streptomycin, were purchased from Sigma-Aldrich (USA). Grids and supports of copper and ammonium molybdate were obtained from Electron Microscopy Sciences (USA).

Synthesis of PEGylated Polyamine (PEG_x-PAH): PAH was modified with PEG chains at different PEG_x:PAH molar ratios: 0.1, 1, and 10 PEG molecule per polyamine chain. In brief, 40 µL of 500 mg mL^{-1} PAH stock solution were added to 50 mL falcon tubes containing 18.4, 18, and 13.5 mL of MilliQ H$_2$O for samples with molar ratios 0.1, 1, and 10, respectively, to a final PAH concentration of 1 mg/mL (6.7×10^{-5} M, 15 000 M_W). The pH of the solution was adjusted to 8 by dropwise addition of 1.5 mL of 0.1 M NaOH solution, to trigger the reaction between the *N*-hydroxysuccinimide esters present on the PEG chains and the amine groups of PAH. Finally, 50, 500, or 5000 µL of 13.30 mg mL^{-1} PEG (2.66 mM, 5000 M_W) were added in DMSO stock solution to obtain a final volume of 20 mL and a PEG concentration of 0.0332, 0.332, and 3.32 mg mL^{-1}, respectively. Reactions were carried out at room temperature and then placed at 4 °C for 4 h under stirring. Solutions were dialyzed against 100 mL of MilliQ H$_2$O using a dialysis cassette with a molecular weight cut-off of 10 kDa to remove the excess of PEG (dialysis water was exchanged three times, after 30 min, 90 min and over-night dialysis). The dialyzed solutions were lyophilized for 48 h resulting in white cotton like powders, stored afterward at −20 °C.

Dynamic Light Scattering: Dynamic light scattering measurements were carried out with a Malvern ζ-Sizer Instrument in backscattering mode. All studies were performed at a 173° scattering angle, temperature controlled at 25 °C in 1 mL polystyrene cuvettes. PANs were characterized in terms of size and ζ-potential. Short time measurements were carried out over 15 min, with three consecutive measurements for each sample. ζ-potential measurements were performed in auto-mode at 25 °C, with three consecutive measurements per sample.

Transmission Electron Microscopy: For transmission electron microscopy analysis of PEGylated PANs, normal and ultra-thin carbon film coated grids were used. 2 µL of undiluted PEG_{10}:PAH with concentration of 2 mg mL^{-1} (assembled 30 min prior to grid deposition of samples) were transferred to plasma coated grids and incubated for 1 min, followed by washing with degassed Nanopure water, incubation with 3 µL of ammonium molybdate 20 mg mL^{-1} for 1 min, and three final washes with degassed Nanopure water. Transmission electron microscopy analysis was performed by using a JEOL JEM 1010 microscope operating at an acceleration voltage of 120 kV.

Small Angle X-Ray Scattering: Small angle X-ray scattering (SAXS) experiments were performed at the Austrian SAXS beamline at the Elettra Synchrotron, Trieste, Italy.[26] Measurements were carried out at 20 °C in an auto-sampler developed in the beamline: the µ-Drop sample changer µDrop: a system for high-throughput SAXS measurements of microliter samples.[27] The µ-Drop system had several advantages over a capillary based setup, the most important being that because just a single drop was placed, the used volume was 15 µL in a capillaries of 1.5 mm outer diameter/0.01 mm wall thickness made from borosilicate (Hilgenberg, Maisfeld, Germany), enclosed within a thermostatic compartment connected to an external circulation bath and a thermal probe for temperature control. A Pilatus3 1 M detector system based on the CMOS hybrid pixel technology recorded the bidimensional patterns, stored in TIF format and then processed with FIT2D[28] and Igor Pro (WaveMetrics, Lake Oswego, OR, USA) software. In detail, the incident and transmitted intensities were measured, data were corrected for sample transmission and fluctuations of the primary beam, each scattering patterns from all images of each sample were averaged and the respective backgrounds, treated in the same way, were subtracted. Scattering patterns were converted to absolute intensity by rescaling the forward intensity with

BSA solution (5.0 mg mL^{-1} in phosphate buffer) and water scattering. 2D detector images were radially averaged to obtain the scattering intensity as a function of the magnitude of the scattering vector Q defined as $Q = 4\pi \sin\theta/\lambda$, with 2θ being the scattering angle and λ equal to 0.154 nm the X-ray wavelength (corresponding to an energy of 8 keV). At least three different volumes of the same sample were measured and at least four times each volume, with an acquisition time of 20 s and a rest time of 3 s for each step. According to this procedure it was aimed to reduce the possibility to induce radiation damage. Raw data were radially averaged and calibrated in absolute units (cm^{-1}) by using a freshly prepared BSA solution (5.0 mg mL^{-1}) in phosphate buffer and water. The sample-to-detector distance was set to 1.247 m, which provided wavenumbers Q by the equation $Q = 4\pi \sin\theta/\lambda$, with 2θ being the scattering angle and λ equal to 1.54 Å the X-ray wavelength. Both polymers solutions (at concentration $c = 1.0$ mg mL^{-1}) and buffers were measured at the same conditions concerning temperature and exposure time. SAXS data analysis was based on a core–shell model, according to Equation (1):

$$\frac{d\Sigma}{d\Omega} = n_{NP}\left\{\frac{4}{3}\pi\left[(\rho_{PEG} - \rho_0)(R+\delta)^3\phi(Q(R+\delta)) + (\rho_{PANS} - \rho_{PEG})R^3\phi(QR)\right]\right\}^2$$
(1)

with $\phi(x) = 3\dfrac{\sin x - x\cos x}{x^3}$ n_{NP} is the nanoparticle number density, ρ_{PEG}, ρ_0, and ρ_{PANS} are the outer shell, the bulk, and the PANs electron densities, respectively, R is the PAN average radius, and δ is the external shell thickness. The average radius of PANs has been considered polydisperse, in agreement with DLS results, according to GENFIT software procedures,[29] the software used to fit the experimental SAXS data.

Fluorescence Correlation Spectroscopy: Green Rhodamine labelled PAH (G-PAH) and green Rhodamine labelled PEG_{10}:PAH were dissolved in MilliQ H$_2$O to a final concentration of 10 mg mL^{-1} of. 3 µL of this stock solution were diluted in 270 µL of 5 mM PBS, in order to allow nanoparticle formation, non-PEGylated and PEGylated PANs respectively. PAH labeled with green rhodamine (G-PAH) was provided by Surflay AC, Germany. Green labelled PEG_{10}:PAH was prepared by PEGylation of G-PAH with 10 PEG chains as described for the nonlabelled PAH. Nanoparticles were then suspended in a solution with BSA in Milli-Q H$_2$O to study the formation of the shell protein. The final concentration of BSA was 800 µM. Nanoparticles were kept for 1 h at 37 °C under stirring at 200 rpm. FCS measurements were performed with the LSM510 confocal microscope from Zeiss and data acquisition was performed with Zen black software. The laser source was a DPSS 561-10 laser with a wavelength of 561 nm and a 40 C Apo/1.2 W DICIII with water immersion objective. The confocal volume was calibrated with Rhodamine B (50 nM) and its known diffusion coefficient of 4.50×10^{-6} cm^2 s^{-1}.[30] Each measurement consisted of at least 10 runs each one of 10 s. FCS data evaluation was done with the open-source software QuickFit. Autocorrelation functions were fitted with a 2 components 3D diffusion model and by using the fit algorithm Simulated Annealing and Levenberg-Marquardt.[31]

Cell Culture: Human lung adenocarcinoma (A549) and breast cancer (4T1) cell lines were cultured with RPMI 1640 medium supplemented with 10% v:v fetal bovine serum (FBS) and 1% v:v antibiotic solution (100 units mL^{-1} penicillin, 100 mg mL^{-1} streptomycin, P/S). Cells were maintained at 37 °C, 5% CO$_2$ in a humidified chamber. Cervical cancer cell lines (HeLa) were cultured with DMEM medium supplemented with 10% of FBS, 1% P/S.

Cell Viability MTT Assay: Cell mitochondrial activity was tested using the 3-(4,5-dimethylthiazol-2-yl)-2,5-diphenyl tetrazolium bromide (MTT) assay, which was based on the mitochondrial conversion of the tetrazolium salt into a formazan dye with absorption characteristics in the visible region. PANs were incubated with cells at different concentrations and different time points (3–48 h). Following incubation with PEGylated PANs at each time point, cells were washed and 135 µL fresh medium with 15 µL of MTT (at 5 mg mL^{-1} in PBS) were added to each well. Nonfunctionalized PAH was used as a control. Culture plates were then incubated at 37 °C. After 2 h incubation, medium-containing MTT was discarded and formazan crystals were dissolved in 150 µL

DMSO. The absorbance at 550 nm (with automatic discount of ref wavelength 630 nm) of the resulting solution was measured in a 96-well spectrophotometer microplate reader. Percentage cell mitochondrial activity was determined by the following formula: (Absorbance of treated cells/ Absorbance of control cells) × 100%.

Synthesis of 6-[18F] Fluoronicotinic Acid 2,3,5,6-Tetrafluorophenyl Ester ([18F]F-PyTFP): [18F]fluorine was produced in a cyclotron (18/9 MeV Cyclone, IBA, Belgium) by proton irradiation of an 18O-enriched water target via the 18O(p, n)18F nuclear reaction. [18F]F-PyTFP was synthesized using a TRACERlab FX-FN synthesis module (GE Healthcare), following a previously reported method. In brief, aqueous [18F] fluoride was first trapped in an ion-exchange resin (Sep-Pak Accell Plus QMA Light) and subsequently eluted to the reactor vessel with a solution of Kryptofix $K_{2.2.2}$/K_2CO_3 in a mixture of water and acetonitrile. After azeotropic drying of the solvent, a solution of F-PyTFP (10 mg) in a mixture of tert-butanol and acetonitrile (4/1) was added and the mixture heated to 40 °C for 15 min. The reaction mixture was then diluted with 1 mL of acetonitrile and 1 mL of water, and purified by HPLC using a Nucleosil 100–7 C18 column (Machery-Nagel, Düren, Germany) as the stationary phase and 0.1% TFA/acetonitrile (25/75) as the mobile phase at a flow rate of 3 mL min⁻¹. The desired fraction (22-23 min [18F]F-PyTFP) was collected, diluted with water (25 mL), and flushed through a C18 cartridge (Sep-Pak Light, Waters) to selectively retain [18F]F-PyTFP. The desired labelled specie was finally eluted with acetonitrile (1 mL). Radiochemical purity was determined by radio-HPLC using a Mediterranean C18 column (4.6 × 150 mm, 5 μm) as the stationary phase and 0.1% TFA/acetonitrile (0–1 min 25% acetonitrile; 9–12 min 90% acetonitrile; 13–15 min 25% acetonitrile) as the mobile phase at a flow rate of 1.5 mL min⁻¹ (retention time: 8 min).

Radiolabeling and Formation of PANs with [18F]F-PyTFP: The radiofluorination of PANs was carried out by the reaction between the free amine groups from PAH and [18F]F-PyTFP. In brief, 200 μL of PAH in 1 M TRIS buffer pH 8 (1 mg mL⁻¹) and 5 μL of [18F]F-PyTFP in acetonitrile (140 ± 10 MBq) were mixed and incubated at room temperature for 5 min. After incubation, the reaction mixture was purified by size exclusion chromatography using Illustra Nap-5 Sephadex columns G-25 DNA grade (GE Healthcare, USA), preconditioned in 5 mM PBS buffer pH 7.4. The fractions containing pure labelled compound were collected, measured in a dose calibrator, and determined by radio-thin layer chromatography (radio-TLC) using iTLC-SG chromatography paper (Agilent Technologies, CA, USA) and dichloromethane and methanol (2/1) as the stationary and mobile phases, respectively. TLC plates were analyzed using TLC-reader (MiniGITA, Raytest). 18F-labelled PANs were synthetized during the purification step (1 mg mL⁻¹ PAH in 5 mM PBS). The same methodology described above was followed for the radiolabeling and formation of PANs with the PEG modification. Instead of 5 mM PBS, 10 mM PBS pH 7.4 was used for the formation of the nanoparticles.

Animals: Female mice (BALB/cJRj, 10 weeks, Janvier; 6 animals) weighing 22 ± 2 g were used to conduct the biodistribution studies. The animals were maintained and handled in accordance with the Guidelines for Accommodation and Care of Animals (European Convention for the Protection of Vertebrate Animals Used for Experimental and Other Scientific Purposes) and internal guidelines. All experimental procedures were approved by the ethical committee and the local authorities before conducting experimental work (Code: PRO-AE-SS-059).

In Vivo Biodistribution Studies in Mice: Animals were anesthetized by inhalation of 3% isoflurane in pure O_2 and maintained by 1.5–2% isofluorane in 100% O_2. 18F-PANs/-PANs-PEG were administered intravenously (2.7 ± 0.4 MBq, 110 μL, 22 ± 2 μg of NP, injected via one of the lateral tails veins) using 5- or 10-mM PBS pH 7.4 as a vehicle (*n* = 3 per NP type). Dynamic, whole body 30-min PET scans were started immediately after administration of the labelled compound and static 10-min PET scans were performed at *t* = 2 and 4 h after administration using the MOLECUBES *β*-CUBE (PET) scanner. After each PET scan, whole body, high resolution CT acquisitions were performed on the MOLECUBES X-CUBE (CT) scanner to provide anatomical information of each animal as well as the attenuation map for later image reconstruction. Random and scatter corrections were automatically applied during image reconstruction (3D OSEM reconstruction algorithm). PET-CT images of the same mouse were co-registered and analyzed using the PMOD image processing tool. Volumes of interest (VOIs) were manually delineated on selected organs (brain, lungs, liver, stomach, kidneys, spleen, and bladder). To obtain an estimation of the concentration of radioactivity in the blood, a VOI was drawn on the heart. Time–activity curves (decay corrected) were obtained as cps cm⁻³ in each organ. Curves were transformed into real activity (Bq cm⁻³) curves by using a calibration factor, obtained from previous scans performed on a phantom (micro-deluxe, Data spectrum Corp.) under the same experimental conditions (isotope, reconstruction algorithm, and energetic window). 3D images were obtained by a 3D image analysis cloud service developed by Multimodal 3D L.L.C.[32]

Supporting Information

Supporting Information is available from the Wiley Online Library or from the author.

Conflict of Interest

The authors declare no conflict of interest.

Author Contributions

P.A. and S.E.M. conceived and designed the study. J.M.P and M.A.R. synthesized and characterized by TEM PEGylated PANS. C.S. performed radioactive labelling and PET/CT scans and data analysis. P.A. did DLS experiments. L.T. did cell viability studies. T.L. measured FCS. H.A., P.A., M. G. O., and S.E.M. conducted SAXS experiments. P.M. and M.G.O. analyzed SAXS data. P.A., M.M., M.G.O., S.E.M., and J.L. analyzed and discussed the data. P.A. and S.E.M. have written this manuscript. All authors have read and approved the final manuscript.

Data Availability Statement

The data that support the findings of this study are available from the corresponding author upon reasonable request.

[1] W. A. Marmisollé, J. Irigoyen, D. Gregurec, S. Moya, O. Azzaroni, *Adv. Funct. Mater.* **2015**, *25*, 4144.

[2] V. S. Murthy, R. R. Rana, M. S. Wong, *J. Phys. Chem. B* **2006**, *110*, 25619.

[3] K. Lutz, C. Grger, M. Sumper, E. Brunner, *Phys. Chem. Chem. Phys.* **2005**, *7*, 2812.

[4] M. L. Agazzi, S. E. Herrera, M. L. Cortez, W. A. Marmisollé, M. Tagliazucchi, O. Azzaroni, *Chem. - Eur. J.* **2020**, *26*, 2456.

[5] S. E. Herrera, M. L. Agazzi, M. L. Cortez, W. A. Marmisollé, M. Tagliazucchi, O. Azzaroni, *Chem. Phys. Chem.* **2019**, *20*, 1044.

[6] P. Andreozzi, E. Diamanti, K. R. Py-Daniel, P. R. Cáceres-Vélez, C. Martinelli, N. Politakos, A. Escobar, M. Muzi-Falconi, R. Azevedo, S. E. Moya, *ACS Appl. Mater. Interfaces* **2017**, *9*, 38242.

[7] D. Di Silvio, M. Martínez-Moro, C. Salvador, M. A. Ramirez, P. R. Cáceres-Vélez, M. G. Ortore, D. Dupin, P. Andreozzi, S. E. Moya, *J. Colloid Interface Sci.* **2019**, *557*, 757.

[8] A. E. Pegg, *Chem. Res. Toxicol.* **2013**, *26*, 1782.

[9] O. Boussif, T. Delair, C. Brua, L. Veron, A. Pavirani, H. V. J. Kolbe, *Bioconjugate Chem.* **1999**, *10*, 877.

[10] J. H. Yu, J. Huang, H. L. Jiang, J. S. Quan, M. H. Cho, C. S. Cho, *J. Appl. Polym. Sci.* **2009**, *112*, 933.

[11] S. Lowe, N. M. O'Brien-Simpson, L. A. Connal, *Polym. Chem.* **2015**, *6*, 198.

[12] H. Otsuka, Y. Nagasaki, K. Kataoka, *Adv. Drug Delivery Rev.* **2003**, *55*, 403.

[13] L. E. van Vlerken, T. K. Vyas, M. M. Amiji, *Pharm. Res.* **2007**, *24*, 1405.

[14] J. Kučka, H. Macková, V. Lobaz, P. Francová, V. Herynek, T. Heizer, P. Páral, L. Šefc, *Sci. Rep.* **2019**, *9*, 10765.

[15] W. Celentano, J. Battistella, I. Proietti Silvestri, R. Bruni, X. Huang, M. Li, P. Messa, S. Ordanini, F. Cellesi, *React. Funct. Polym.* **2018**, *131*, 164.

[16] K. K. Gill, A. Kaddoumi, S. Nazzal, *J. Drug Target* **2014**, *23*, 222.

[17] K. Knop, R. Hoogenboom, D. Fischer, U. S. Schubert, *Angew. Chem., Int. Ed.* **2010**, *49*, 6288.

[18] R. Michel, S. Pasche, M. Textor, D. G. Castner, *Langmuir* **2005**, *21*, 12327.

[19] R. Gref, Y. Minamitake, M. T. Peracchia, V. Trubetskoy, V. Torchilin, R. Langer, *Science* **1994**, *263*, 1600.

[20] C. Röcker, M. Pötzl, F. Zhang, W. J. Parak, G. U. Nienhaus, *Nat. Nanotechnol.* **2009**, *4*, 577.

[21] P. Andreozzi, C. Ricci, J. E. M. Porcel, P. Moretti, D. Di Silvio, H. Amenitsch, M. G. Ortore, S. E. Moya, *J. Colloid Interface Sci.* **2019**, *543*, 335.

[22] M. Maccarini, G. Briganti, S. Rucareanu, X. Lui, R. Sinibaldi, M. Sztucki, B. Lennox, *J. Phys. Chem. C* **2010**, *114*, 6937.

[23] M. P. Monopoli, C. Åberg, A. Salvati, K. A. Dawson, *Nat. Nanotechnol.* **2012**, *7*, 779.

[24] S. Jazani, I. Sgouralis, O. M. Shafraz, M. Levitus, S. Sivasankar, S. Pressé, *Nat. Commun.* **2019**, *10*, 3662.

[25] E. L. Elson, *Biophys. J.* **2011**, *101*, 2855.

[26] H. Amenitsch, M. Rappolt, M. Kriechbaum, H. Mio, P. Laggner, S. Bernstorff, *J. Synchrotron Radiat.* **1998**, *5*, 506.

[27] R. Haider, B. Sartori, A. Radeticchio, M. Wolf, S. Dal Zilio, B. Marmiroli, H. Amenitsch, *J. Appl. Crystallogr.* **2021**, *54*, 132.

[28] A. P. Hammersley, K. Brown, W. Burmeister, L. Claustre, A. Gonzalez, S. McSweeney, E. Mitchell, J. P. Moy, S. O. Svensson, A. W. Thompson, *J. Synchrotron Radiat.* **1997**, *4*, 67.

[29] F. Spinozzi, C. Ferrero, M. G. Ortore, A. De Maria Antolinos, P. Mariani, *J. Appl. Crystallogr.* **2014**, *47*, 1132.

[30] P. O. Gendron, F. Avaltroni, K. J. Wilkinson, *J. Fluoresc.* **2008**, *18*, 1093.

[31] A. Silvestri, D. Di Silvio, I. Llarena, R. A. Murray, M. Marelli, L. Lay, L. Polito, S. E. Moya, *Nanoscale* **2017**, *9*, 14730.

[32] R. Sinibaldi, A. Conti, B. Sinjari, S. Spadone, R. Pecci, M. Palombo, V. S. Komlev, M. G. Ortore, G. Tromba, S. Capuani, R. Guidotti, F. De Luca, S. Caputi, T. Traini, S. D. Penna, *J. Tissue Eng. Regener. Med.* **2018**, *12*, 750.